

Automatic Design of High-Sensitivity Color Filter Arrays With Panchromatic Pixels

Jia Li, Chenyan Bai, Zhouchen Lin, *Senior Member, IEEE*, and Jian Yu

Abstract—In most of existing digital cameras, color images have to be reconstructed from raw images, which only have one color sensed at each pixel, as their imaging sensors are covered by color filter arrays (CFAs). At each pixel, a CFA usually allows only a portion of the light spectrum to pass through, and thereby reduces the light sensitivity of pixels. To address this issue, previous works have explored adding panchromatic pixels into CFAs. However, almost all existing methods assign panchromatic pixels *empirically*, making the designed CFAs prone to aliasing artifacts. In this paper, *based on a mathematical model*, we propose a *fully automatic* approach to designing high-sensitivity CFAs using panchromatic pixels. By the frequency structure representation of CFAs, we formulate high-sensitivity CFA design as a continuous multi-objective optimization problem, where robustness to aliasing artifacts and percentage of panchromatic pixels are simultaneously maximized. We analyze the characteristics of our new formulation. According to the analysis, we develop a new method to propose frequency structure candidates, which can produce CFAs that reach a desired percentage of panchromatic pixels. Then for each candidate, we optimize parameters to obtain the final CFA, which is an appropriately balanced solution to the multi-objective optimization problem. We formulate the two design procedures as constrained optimization problems and solve them using the alternating direction method. Extensive experiments confirm the advantage of the proposed method in both low-light and normal-light conditions.

Index Terms—Color filter array (CFA), demosaicking, high-sensitivity, panchromatic pixels, aliasing, continuous multi-objective optimization, alternating direction method (ADM).

Manuscript received May 3, 2016; revised September 7, 2016; accepted November 25, 2016. Date of publication November 30, 2016; date of current version December 19, 2016. The work of C. Bai was supported by the National Natural Science Foundation of China under Grant 61402462. The work of Z. Lin was supported in part by the 973 Program of China under Grant 2015CB352502 and in part by the National Natural Science Foundation of China under Grant 61625301 and Grant 61231002. The work of J. Yu was supported by the National Natural Science Foundation of China under Grant 61632004 and Grant 61370129. The associate editor coordinating the review of this manuscript and approving it for publication was Dr. Vladimir Stankovic.

J. Li and J. Yu are with the Beijing Key Laboratory of Traffic Data Analysis and Mining, School of Computer and Information Technology, Beijing Jiaotong University, Beijing 100044, P.R. China (e-mail: jiali.gm@gmail.com; jianyu@bjtu.edu.cn).

C. Bai is with the Beijing Advanced Innovation Center for Imaging Technology, College of Information Engineering, Capital Normal University, Beijing 100048, P.R. China (e-mail: cybai@cnu.edu.cn).

Z. Lin is with the Key Laboratory of Machine Perception (Ministry of Education), School of Electronics Engineering and Computer Science, Peking University, Beijing 100871, P.R. China, and also with the Cooperative Medianet Innovation Center, Shanghai Jiao Tong University, Shanghai 200240, P.R. China (e-mail: zlin@pku.edu.cn).

This paper has supplementary downloadable material available at <http://ieeexplore.ieee.org/>, provided by the author.

Color versions of one or more of the figures in this paper are available online at <http://ieeexplore.ieee.org>.

Digital Object Identifier 10.1109/TIP.2016.2633869

I. INTRODUCTION

MOST digital cameras produce color images by using a single sensor covered by a color filter array (CFA). A CFA has the same size as the sensor and usually allows only one color spectrum to pass through at each pixel. So every pixel of the images obtained with a CFA has only one color component. Such images are called raw images. Since color images contain at least three color components (e.g., red (R), green (G), and blue (B)) at each pixel, demosaicking algorithms are needed to reconstruct color images from raw images [1]–[3]. Accordingly, both the CFA and the demosaicking algorithm are crucial to the quality of the reconstructed color images. Instead of developing sophisticated demosaicking algorithms, in this paper we concentrate on CFA design. We only consider periodic CFAs defined on the square lattice, in which the minimum periodic arrays are called CFA patterns. For non-periodic CFAs, we refer the readers to [4].

The Bayer CFA [5] is the most widely used CFA in the consumer market. As shown in Fig. 1(1a), it is a 2×2 CFA pattern and has twice green components as red and blue ones, which is based on the fact that human visual system (HVS) is more sensitive to green light. Despite the popularity, it has two fundamental limitations. First, spectral characteristic analysis [14] shows that the chrominance components (chroma for short) of the raw images by Bayer CFA locate on the horizontal and the vertical axes, where the luminance component (luma for short) has a high density (see Fig. 1(2a)). So the aliasing artifacts resulting from spectral overlap are inevitable. Since imaging with a CFA is a sampling process, the robustness to aliasing artifacts is a crucial criterion in CFA design. This criterion has been well established by the design of CFAs in the frequency domain [12], [15], [16]. It is important to note that the luma and chromas used in this paper, resulting from raw images, are not directly related to the usual definition of luma and chromas used in image and video processing (e.g., YCrCb or YIQ). In the frequency domain, a raw image by a CFA can be interpreted as the sum of a non-subsampled component at the baseband and multiple subsampled replicas of components at the high frequency bands, where the non-subsampled component is called luma and the subsampled ones are called chromas. We show the spectra of raw images by six existing CFAs in the second row of Fig. 1, where the luma and chromas are denoted by the black and the white dashed circles, respectively. Moreover, all the frequency information of raw images by a CFA can be recorded by a matrix called frequency structure

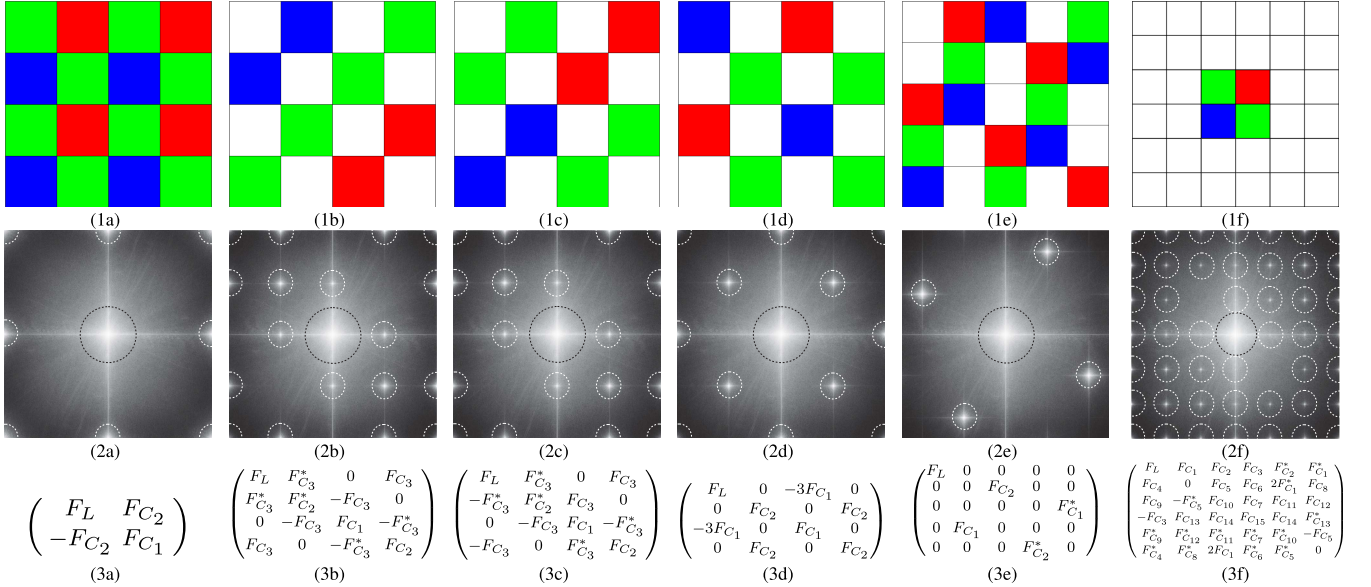


Fig. 1. Six existing CFA patterns and their corresponding spectra and frequency structures. The first row are the (a) Bayer CFA [5], (b) Compton CFA [6], (c) Kumar CFA [7], (d) Honda CFA [8], (e) Wang CFA [9], and (f) Chakrabarti CFA [10], respectively. The sum across color channels of every CFA is normalized to be an all-one matrix. In particular, the three color values of a panchromatic pixel are all 1/3. The second row are the average spectra of all raw images from the Kodak dataset [11] whose corresponding CFAs are in the first row. From the second row, we can clearly see that the luminance spectrum is located in the center and on the horizontal and the vertical axes, which is denoted by the black dashed circle. The chrominance spectra are denoted by the white dashed circles. The third row are the corresponding frequency structures [12] of CFAs in the first row, which record the spectral components and their positions in the second row. As noted in [13], the basebands are placed at the center by convention in the second row, but all the Discrete Fourier Transform (DFT) spectra are periodic in both horizontal and vertical directions. However, the frequency origin (0, 0) of every frequency structure in the third row is at the top-left entry of the matrix. **Images in this paper are best viewed on screen!**

(see the third row of Fig. 1), which leads to the frequency structure-based CFA design [12]. Details on this issue are provided in subsection II-A. The second limitation of the Bayer CFA is that it blocks roughly two-thirds of the incident light [7], [8], [10]. So color cameras with the Bayer CFA are significantly slower than their grayscale counterparts, making the obtained raw images blurrier when capturing in the presence of camera or object movements. Also, the significant loss of light limits the ability of Bayer CFA in trading off noise, exposure time, and aperture size, especially in low-light conditions.

In recent years, alleviating the second shortcoming of Bayer CFA has been an attractive topic. Many color image enhancement algorithms for deblurring [17]–[20] and denoising [21]–[24] of low-light scenes have been presented. There are also hardware design approaches [25]–[28]. Our work essentially belongs to this category. But our goal is to design high light-sensitivity CFAs without sacrificing color fidelity. Actually, this problem has been studied by some researchers [6]–[10] by including panchromatic (P) pixels in CFAs. As panchromatic pixels do not block the visible light, a larger percentage of panchromatic pixels implies a higher sensitivity of the CFA. More importantly, the implementation of a CFA with panchromatic pixels is practicable, which has been discussed in detail [27].

However, most high-sensitivity CFAs assign panchromatic pixels *empirically*. For example, Compton and Hamilton, Jr., [6] and Kumar *et al.* [7] proposed two similar CFAs, both of which include 50% panchromatic pixels (Fig. 1 (1b) and (1c)). The two CFAs were shown to perform

better than the Bayer CFA in capturing under low light, reducing motion blur, and decreasing noise level. Honda *et al.* [8] presented a CFA with 50% panchromatic pixels (Fig. 1(1d)). In low-light conditions, their CFA was demonstrated to produce higher signal-to-noise ratio (SNR) than the Bayer CFA does. However, these high-sensitivity CFAs are prone to aliasing artifacts. From the spectra of raw images by these CFAs shown in Fig. 1 (2b)–(2d), we can see that the chromas and luma overlap on the horizontal and the vertical axes.

There are some systematic methods to assign panchromatic pixels. Motivated by the geometric CFA design method in [12], Wang *et al.* [9] proposed a new high-sensitivity CFA, which is also robust to aliasing artifacts. They first *empirically* specified a good frequency structure. Then they used the geometric method to optimize parameters with a constraint that the color components of the CFA can only be R, G, B, and P. The designed CFA was shown to outperform the Compton CFA [6] on the Kodak dataset [11]. Their CFA and its corresponding spectrum are shown in Fig. 1 (1e) and (2e), respectively. We can see that it includes 40% panchromatic pixels and has no spectral overlap. However, they did not give details of generating the panchromatic pixels, and the geometric design method did not limit the used color components [12]. Moreover, as shown in Fig. 2 (b)–(e), their specified frequency structure can produce four different percentages of panchromatic pixels, which correspond to different trade-offs between robustness to aliasing artifacts and light sensitivity. This also needs to be treated in CFA design. Additionally, their frequency structure selection and parameter optimization both require *human involvement* [12], [13].

Inspired by the success in inpainting and colorization, Chakrabarti *et al.* [10] co-designed the CFA with panchromatic pixels and the reconstruction algorithm. In their CFA, the non-panchromatic pixels account for a low percentage (about 11%) and concentrate in the center, which are surrounded by panchromatic pixels (Fig. 1(1f)). Consequently, their reconstruction algorithm first inpainted the missing panchromatic values at the non-panchromatic pixels. Then it estimated color information from the non-panchromatic pixels and next colored the panchromatic pixels. Their approach was shown to outperform the Bayer CFA demosaicked by the directional LMMSE algorithm [29] in reducing noise and aliasing artifacts under low light. However, they directly place a 2×2 Bayer CFA pattern in the center of their 6×6 CFA pattern (see Fig. 1(1f)). From the corresponding spectrum shown in Fig. 1(2f), we can see that there exists severe spectral overlap.

Recently, based on the frequency structure, Bai *et al.* [13] proposed a new CFA design method in the frequency domain, which is fully automatic. However, like all existing spectral design methods [12], [15], [16], it only considers reducing aliasing artifacts and neglects enhancing light sensitivity with panchromatic pixels. In this paper, we extend the method presented in [13] to design high-sensitivity CFAs using panchromatic pixels, which is *more challenging* than the traditional CFA design. First, it should still enhance the robustness to aliasing artifacts. However, traditional CFA design optimizes parameters without constraining all the color components used, while high-sensitivity CFA design needs to use panchromatic pixels although other color components are still unconstrained. Second, the three color values of a panchromatic pixel are all $1/3$, which should be precisely generated. However, the locations of panchromatic pixels are unknown *a priori*. Third, the percentage of panchromatic pixels should be considered in the design (actually, it should be above a given threshold). This is because it determines the trade-off between light sensitivity and color fidelity. In order to handle these issues, we formulate high-sensitivity CFA design as a continuous multi-objective optimization problem. The two objectives are the robustness to aliasing artifacts and the percentage of panchromatic pixels, which conflict with each other. Namely, optimizing one objective can make the other worse, e.g., the all-panchromatic CFA achieves the highest sensitivity at the expense of losing all color information. In general, solving continuous multi-objective optimization is challenging when there exists conflict among objectives [30]. However, we show that the key property making our formulation tractable is the finite discrete range of one objective function. According to the analysis, we propose a new high-sensitivity CFA design method, which consists of two steps, frequency structure selection and parameter optimization.

The contributions of this paper are:

- Based on the frequency structure representation of CFAs, we formulate high-sensitivity CFA design with panchromatic pixels as a continuous multi-objective optimization problem. To the best of our knowledge, it is the first panchromatic pixel assignment method with a mathematical model, which is also fully automatic.

TABLE I
SUMMARY OF THE MAIN NOTATIONS USED IN THIS PAPER

Notation	Definition
\mathbb{R}, \mathbb{R}_+	Set of real and nonnegative real numbers, respectively
\mathbb{C}	Set of complex numbers
$\mathbf{1}$	All-one vector or matrix
$\mathbf{0}$	All-zero vector or matrix
\mathbf{I}	Identity matrix
$[\mathbf{x}]_j$	j -th element of vector \mathbf{x}
$\text{diag}(\mathbf{x})$	Diagonal matrix whose j -th diagonal element is $[\mathbf{x}]_j$
$[\mathbf{X}]_{jk}$	(j, k) -th element of matrix \mathbf{X}
$[\mathbf{X}]_{j,:}$	j -th row of matrix \mathbf{X}
$[\mathbf{X}]_{:,k}$	k -th column of matrix \mathbf{X}
$\text{vec}(\mathbf{X})$	Vector formed by stacking all the columns of matrix \mathbf{X}
\mathbf{X}^T	Transpose of matrix \mathbf{X}
\mathbf{X}^H	Conjugate transpose of matrix \mathbf{X}
$\Re(\cdot)$	Real part of a complex vector or matrix
$\Im(\cdot)$	Imaginary part of a complex vector or matrix
\mathbf{X}^{-1}	Inverse of matrix \mathbf{X}
\mathbf{X}^\dagger	Pseudo-inverse of matrix \mathbf{X}
$\ \mathbf{x}\ _0$	ℓ_0 -norm (number of nonzero elements) of vector \mathbf{x}
$\ \mathbf{x}\ _2$	ℓ_2 -norm ($\sqrt{\sum_j [\mathbf{x}]_j^2}$) of vector \mathbf{x}
$\ \mathbf{x}\ _\infty$	ℓ_∞ -norm ($\max_j \{ \mathbf{x} _j\}$) of vector \mathbf{x}
$\ \mathbf{X}\ _F$	Frobenius norm ($\sqrt{\sum_j \sum_k [\mathbf{X}]_{jk}^2}$) of matrix \mathbf{X}
$\ \mathbf{X}\ _\infty$	ℓ_∞ -norm ($\max_{j,k} \{ \mathbf{X} _{jk}\}$) of matrix \mathbf{X}
$\ \mathbf{X}\ _2$	Spectral norm (largest singular value) of matrix \mathbf{X}
$\ \mathbf{X}\ _{2,0}$	$\ell_{2,0}$ -norm (number of nonzero columns) of matrix \mathbf{X}

Note that ℓ_0 -norm and $\ell_{2,0}$ -norm are not true norms because they do not satisfy the positive scalability: $\|\alpha \mathbf{x}\|_0 = |\alpha| \|\mathbf{x}\|_0$ and $\|\alpha \mathbf{X}\|_{2,0} = |\alpha| \|\mathbf{X}\|_{2,0}$ for any scalar α . The term “norm” here is for convenience.

- We demonstrate and analyze the challenge of solving the new formulation, which leads to our new parameter optimization method for high-sensitivity CFAs. Our parameter optimization method is flexible for including a constraint that the produced CFA should achieve a given percentage of panchromatic pixels.
- We develop a new approach to propose frequency structure candidates, which discards the frequency structures whose corresponding CFAs cannot reach a given percentage of panchromatic pixels. This guarantees that every candidate has desired light sensitivity. The subsequent parameter optimization then minimizes the aliasing artifacts.

The rest of the paper is organized as follows. In Section II, we describe our multi-objective optimization formulation for designing high-sensitivity CFAs with panchromatic pixels. Then we introduce our high-sensitivity CFA design method in Section III. In Section IV, we conduct experiments to test our design method. Finally, we conclude the paper in Section V.

II. MULTI-OBJECTIVE OPTIMIZATION FORMULATION

In this section, we first briefly introduce the frequency structure, as we will rely on it to design CFAs. Then we give and analyze our multi-objective optimization formulation for designing high-sensitivity CFAs. We use upper and lower case boldface letters to denote matrices and vectors, respectively, where vectors are all column ones. Scalars are denoted by lower case letters. To enable readers to quickly refer to the notations used throughout the paper, we summarize the main notations in Table I.

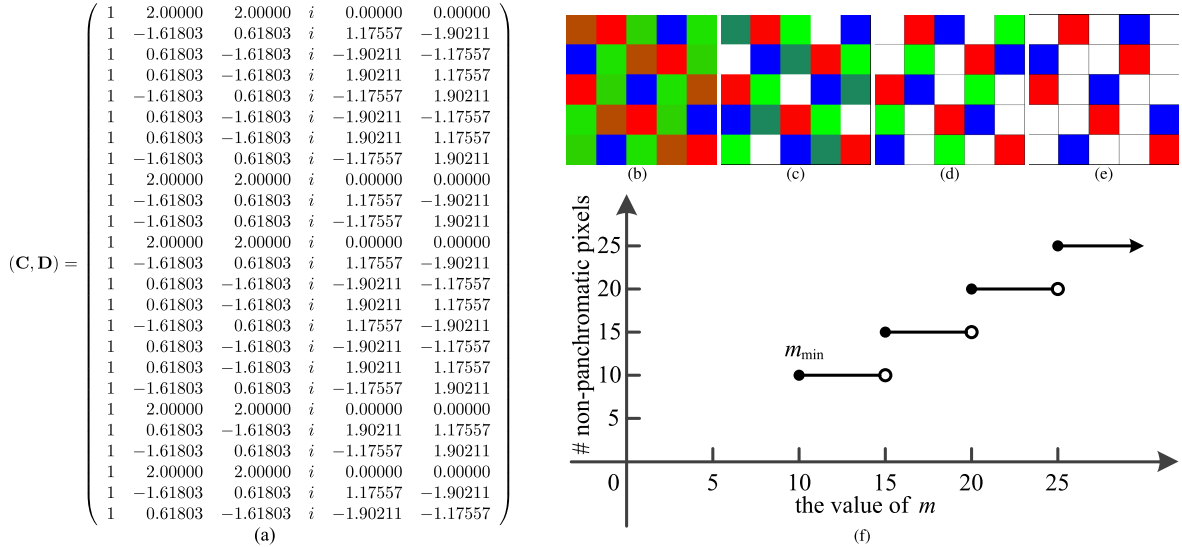


Fig. 2. The characteristics of the frequency structure specified by Wang *et al.* [9]. (a) is its coefficient matrices. (b)-(e) are four CFAs produced by the frequency structure. They are optimal CFAs with 0%, 20%, 40%, and 60% panchromatic pixels, respectively. The corresponding values of $\|\mathbf{M}^{-1}\|_2$ are 3.05, 3.16, 3.51, and 7.53, respectively. (f) is the correspondence between the obtained number of non-panchromatic pixels and m of the model problem in (6), which is a step function w.r.t. m in $[m_{\min}, +\infty)$.

A. Frequency Structure

The frequency structure is a matrix with the same size as the corresponding CFA pattern, which records the positions and relations of all luma and chromas of raw images captured by the CFA (see the third row of Fig. 1) [12]. It is image independent and relies only on the CFA. The frequency structure is attractive for the conversion between it and the CFA pattern is simple. For a given CFA pattern, the frequency structure can be easily computed using the symbolic Discrete Fourier Transform (DFT), which is a standard DFT except treating symbols as parameters [31]. More specifically, by applying the symbolic DFT to a given CFA pattern, we can obtain its frequency structure and the relationship between its frequency components and RGB color components, which is given as:

$$(F_L, F_{C_1}, F_{C_2})^T = \mathbf{M}(R, G, B)^T, \quad (1)$$

where F_L , F_{C_1} , and F_{C_2} denote the luma and the two chromas, respectively, R , G , and B refer to the red, green, and blue color components, respectively, and $\mathbf{M} \in \mathbb{C}^{3 \times 3}$ is invertible and is called the color transformation matrix. Conversely, given a matched color transformation matrix \mathbf{M} , we can obtain the corresponding CFA pattern by applying the inverse symbolic DFT to the frequency structure. So all the CFA patterns with an identical frequency structure can be parameterized by \mathbf{M} . This leads to the frequency-structure-based CFA design [12], [13] described below.

For a given frequency structure (e.g., one of those in the third row of Fig. 1), we first parameterize the complex color transformation matrix \mathbf{M} as $\mathbf{M}_1 + i\mathbf{M}_2$, where \mathbf{M}_1 and \mathbf{M}_2 are the real and imaginary parts of \mathbf{M} , respectively. Then according to (1), we parameterize the frequency structure as \mathbf{M} . We next apply the inverse symbolic DFT to the parameterized frequency structure and obtain the *vectorized* CFA pattern $\mathbf{CR}(\mathbf{M}) + \mathbf{DI}(\mathbf{M})$, where \mathbf{C} and \mathbf{D} are the complex

coefficient matrices. An example of \mathbf{C} and \mathbf{D} is shown in Fig. 2(a). Let \mathbf{K}_j be the j -th channel of the CFA pattern with a size of $n_r \times n_c$, where $j \in \{R, G, B\}$. Then the vectorized CFA pattern is $(\text{vec}(\mathbf{K}_R), \text{vec}(\mathbf{K}_G), \text{vec}(\mathbf{K}_B))$ with a size of $n_r n_c \times 3$. After this, CFA design is converted into the optimization of \mathbf{M} . Since \mathbf{M} is the transformation matrix between two bases (see (1)), it is considered optimal when the numerical stability of color transformation is maximized [12], which can be accomplished by directly minimizing $\|\mathbf{M}^{-1}\|_2$ [13]. By doing so, the robustness to aliasing artifacts of the obtained CFA is maximized. Formally, Bai *et al.* [13] formulated the optimization of \mathbf{M} as follows:

$$\begin{aligned} & \min_{\mathbf{M}} \|\mathbf{M}^{-1}\|_2 \\ & \text{s.t. } \mathbf{Ma} = \mathbf{b}, \mathbf{CR}(\mathbf{M}) + \mathbf{DI}(\mathbf{M}) \geq \mathbf{0}, \end{aligned} \quad (2)$$

where \geq stands for componentwise greater than or equal to, $\mathbf{a} = (1, 1, 1)^T$, and $\mathbf{b} = (1, 0, 0)^T$. The equality constraint guarantees that the sum across color channels of the CFA pattern is an all-one matrix, while the inequality constraint ensures the physical realizability.

B. Proposed Formulation

Based on the frequency structure, we design high-sensitivity CFAs with panchromatic pixels in the frequency domain. According to previous discussion, for a given frequency structure, we have two objectives on the optimality of \mathbf{M} . The first one is that the value of $\|\mathbf{M}^{-1}\|_2$ should be minimized. The second one is that the percentage of panchromatic pixels should be maximized. For a given CFA pattern size, it is equivalent to minimizing the number of non-panchromatic pixels. Let the vectorized CFA pattern be $\mathbf{CR}(\mathbf{M}) + \mathbf{DI}(\mathbf{M})$, then the number of non-panchromatic pixels can be represented as $\|(\mathbf{CR}(\mathbf{M}) + \mathbf{DI}(\mathbf{M}))^T - \frac{1}{3}\mathbf{1}\|_{2,0}$. Following [12], [13], we also enforce the CFA pattern to be physically realizable and

the sum across its color channels to be an all-one matrix. Accordingly, for a given frequency structure, we propose the following model to optimize \mathbf{M} :

$$\begin{aligned} \min_{\mathbf{M}} \quad & \left\{ \|\mathbf{M}^{-1}\|_2, \left\| (\mathbf{C}\mathfrak{R}(\mathbf{M}) + \mathbf{D}\mathfrak{I}(\mathbf{M}))^T - \mathbf{1}/3 \right\|_{2,0} \right\} \\ \text{s.t. } & \mathbf{M}\mathbf{a} = \mathbf{b}, \quad \mathbf{C}\mathfrak{R}(\mathbf{M}) + \mathbf{D}\mathfrak{I}(\mathbf{M}) \geq \mathbf{0}. \end{aligned} \quad (3)$$

It is a continuous multi-objective optimization problem with two objectives.

C. Analysis on Our Formulation

A multi-objective optimization problem results in a set of Pareto-optimal solutions, which need a further decision to get a single preferred one [30]. The Pareto-optimality is defined based on the objective function values of feasible solutions. Formally, we have the following definition:

Definition 1: A feasible solution \mathbf{x}^ is Pareto optimal if there does not exist a feasible solution \mathbf{x} such that \mathbf{x} is no worse than \mathbf{x}^* in all objectives and \mathbf{x} is strictly better than \mathbf{x}^* in at least one objective.*

The finding of all Pareto-optimal solutions becomes challenging when the objectives are in conflict, i.e., minimizing one objective can increase the values of the others. Unfortunately, the two objectives in (3) do conflict each other. Namely, for a given frequency structure, a lower percentage of non-panchromatic pixels often accompanies with a larger value of $\|\mathbf{M}^{-1}\|_2$ (see Fig. 2 (b)-(e)).

One may utilize the frequently used weighting method [30] to solve problem (3). It associates the two objective functions with a weighting coefficient and minimizes their weighted sum. As a result, the two objective functions are transformed into a single one and different Pareto-optimal solutions of problem (3) are obtained by altering the weighting coefficient in the weighted problem. Formally, problem (3) is converted into:

$$\begin{aligned} \min_{\mathbf{M}} \quad & \|\mathbf{M}^{-1}\|_2 + \mu \left\| (\mathbf{C}\mathfrak{R}(\mathbf{M}) + \mathbf{D}\mathfrak{I}(\mathbf{M}))^T - \mathbf{1}/3 \right\|_{2,0} \\ \text{s.t. } & \mathbf{M}\mathbf{a} = \mathbf{b}, \quad \mathbf{C}\mathfrak{R}(\mathbf{M}) + \mathbf{D}\mathfrak{I}(\mathbf{M}) \geq \mathbf{0}, \end{aligned} \quad (4)$$

where $\mu > 0$ is the weighting coefficient. However, the weighting method requires choosing an appropriate μ in (4) to generate the desired Pareto-optimal solution of problem (3). When the solution of the weighted problem is Lipschitz w.r.t. the weighting coefficients, selecting the proper weighting coefficients is trivial [30]. Unfortunately, problem (4) does not meet the requirement of Lipschitz continuity as $\left\| (\mathbf{C}\mathfrak{R}(\mathbf{M}) + \mathbf{D}\mathfrak{I}(\mathbf{M}))^T - \mathbf{1}/3 \right\|_{2,0}$ is a discrete function. Moreover, since problem (3) is non-convex, altering μ in (4) cannot produce all its Pareto-optimal solutions [30], which implies that the desired one may not be found by the weighting method. Note that a multi-objective optimization problem is convex if all the objective functions and the feasible region are convex.

Let \mathcal{R} be the range of $\left\| (\mathbf{C}\mathfrak{R}(\mathbf{M}) + \mathbf{D}\mathfrak{I}(\mathbf{M}))^T - \mathbf{1}/3 \right\|_{2,0}$. It is discrete and finite. So all the Pareto-optimal solutions of problem (3) are among the solutions to the following model

problem:

$$\begin{aligned} \min_{\mathbf{M}} \quad & \|\mathbf{M}^{-1}\|_2 \\ \text{s.t. } & \mathbf{M}\mathbf{a} = \mathbf{b}, \quad \mathbf{C}\mathfrak{R}(\mathbf{M}) + \mathbf{D}\mathfrak{I}(\mathbf{M}) \geq \mathbf{0}, \\ & \left\| (\mathbf{C}\mathfrak{R}(\mathbf{M}) + \mathbf{D}\mathfrak{I}(\mathbf{M}))^T - \mathbf{1}/3 \right\|_{2,0} = l, \end{aligned} \quad (5)$$

for every $l \in \mathcal{R}$. Note that $\mathcal{R} \subset \{2, 3, \dots, n_r n_c\}$. Actually, some integers between 2 and $n_r n_c$ are not in \mathcal{R} . The reasons are as follows. Let the vectorized CFA pattern be $\mathbf{CM}_1 + \mathbf{DM}_2 = (\mathbf{C}, \mathbf{D}) \begin{pmatrix} \mathbf{M}_1 \\ \mathbf{M}_2 \end{pmatrix}$. Then no matter what the value of \mathbf{M} is, the rows having the same values in (\mathbf{C}, \mathbf{D}) result in identical color component. We provide an example in Fig. 2 (a). We can see that (\mathbf{C}, \mathbf{D}) has five unique rows, each of which appears five times. So 2, 6, and 11 are not in \mathcal{R} . On the other hand, different unique rows may also generate identical color component. We can see from Fig. 2(e) that there are three unique rows that produce panchromatic pixels. When the feasibility and invertibility of \mathbf{M} in (3) are further considered, it will be non-trivial to exactly determine \mathcal{R} .

Based on the above observations, we modify the model problem in (5) as follows:

$$\begin{aligned} \min_{\mathbf{M}} \quad & \|\mathbf{M}^{-1}\|_2 \\ \text{s.t. } & \mathbf{M}\mathbf{a} = \mathbf{b}, \quad \mathbf{C}\mathfrak{R}(\mathbf{M}) + \mathbf{D}\mathfrak{I}(\mathbf{M}) \geq \mathbf{0}, \\ & \left\| (\mathbf{C}\mathfrak{R}(\mathbf{M}) + \mathbf{D}\mathfrak{I}(\mathbf{M}))^T - \mathbf{1}/3 \right\|_{2,0} \leq m, \end{aligned} \quad (6)$$

for every $m \in \{m_{\min}, \dots, n_r n_c\}$, where m_{\min} is the minimum number of non-panchromatic pixels that the frequency structure could produce. The model problem in (6) can also generate all the Pareto-optimal solutions of problem (3). As we can see from Fig. 2(f), the obtained number of non-panchromatic pixels by (6) is a step function w.r.t. m . This implies that the model problem in (6) is feasible w.r.t. m in $[m_{\min}, +\infty)$. Accordingly, to solve problem (3), we only need to compute m_{\min} rather than determining \mathcal{R} .

III. PROPOSED DESIGN METHOD FOR HIGH-SENSITIVITY CFAs

Based on our analysis above, we propose a new method to design high-sensitivity CFAs. The whole process of the proposed design method is shown in Fig. 3. It consists of two main steps. For a given CFA pattern size, it first proposes frequency structure candidates (the dashed box in Fig. 3). Then it optimizes parameters for each candidate to obtain a promising CFA. Below we describe the two steps in detail.

A. Propose Frequency Structure Candidates

1) *Generate All Frequency Structures:* Bai *et al.* [13] developed a discrete multi-objective optimization approach to propose the potentially optimal frequency structures in minimizing aliasing artifacts. However, due to the conflict between the robustness to aliasing artifacts and the number of panchromatic pixels, their approach is not applicable in designing high-sensitivity CFAs. So we generate all frequency structures. As shown in Fig. 3(a), the only luma is fixed at the top-left entry of the frequency structure. We only need to specify the replicas of two chromas and their positions

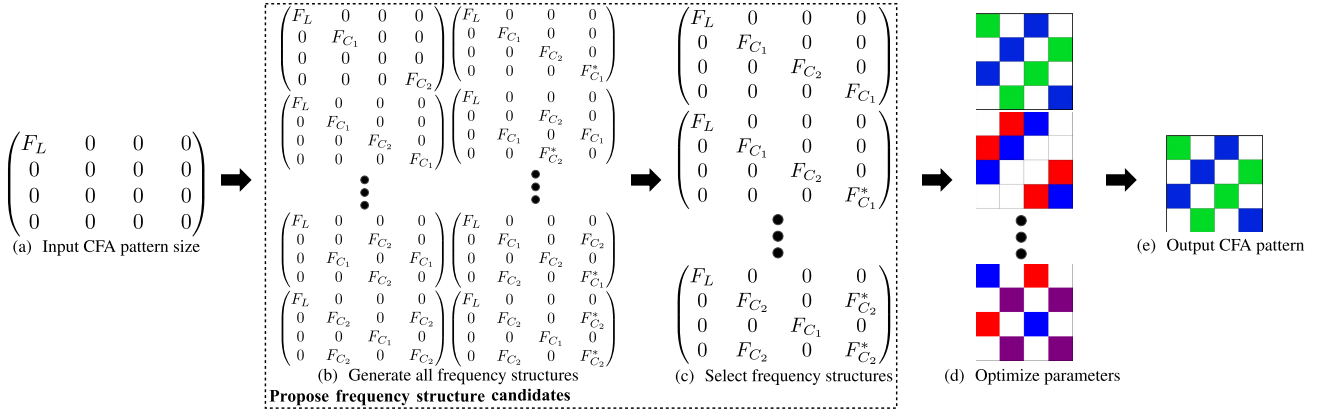


Fig. 3. Overview of the proposed design method for high-sensitivity CFAs. From left to right: (a) is the input CFA pattern size, in which ' F_L ' marks the position of luma and '0' marks the available chroma positions. Our method first generates all frequency structures (b). Then it selects the frequency structures which can produce CFAs reaching a desired percentage of panchromatic pixels (c). For each selected frequency structure, it optimizes parameters to get the designed CFA (d). Note that our method produces a unique CFA for each frequency structure candidate. However, a CFA pattern size often results in multiple frequency structure candidates (see (c)). We only output the CFA with the best demosaicing performance on a training image set (e).

in the matrix to determine a frequency structure. We first obtain all chroma position allocations, and then we generate frequency structures according to them. These two steps have been described in detail in [13]. We discard the frequency structures whose chroma replicas are located on the horizontal and the vertical axes of luma. Moreover, in order to reduce the spectral overlap among chroma replicas, we reject the frequency structures which contain chroma replicas at adjacent positions in the same row or column, as well as those containing more than 5 chroma replicas.

2) Select Frequency Structures: We select frequency structures based on the maximum percentages of panchromatic pixels that they can generate. For a given CFA pattern size, we first compute the minimum number of non-panchromatic pixels m_{\min} of every frequency structure, which is formulated as an optimization problem:

$$\begin{aligned} \min_{\mathbf{M}} & \|(\mathbf{C}\mathfrak{R}(\mathbf{M}) + \mathbf{D}\mathfrak{I}(\mathbf{M}))^T - \mathbf{1}/3\|_{2,0} \\ \text{s.t. } & \mathbf{M}\mathbf{a} = \mathbf{b}, \mathbf{C}\mathfrak{R}(\mathbf{M}) + \mathbf{D}\mathfrak{I}(\mathbf{M}) \geq \mathbf{0}, \\ & \|\mathbf{M}^{-1}\|_2 \leq \nu, \end{aligned} \quad (7)$$

where $\nu > 0$ is a constant. The constraint $\|\mathbf{M}^{-1}\|_2 \leq \nu$ ensures that \mathbf{M} is invertible. Suppose we know the m_{\min} of a frequency structure in advance. Then we let m be m_{\min} in (6) and obtain the optimal solution \mathbf{M}^* . If the pre-set ν is smaller than $\|(\mathbf{M}^*)^{-1}\|_2$, we will not be able to obtain m_{\min} by solving (7). So we set ν to be a sufficiently large number so that \mathbf{M}^* is a feasible solution of problem (7). In all our experiments, we set $\nu = 100$. In order to improve the readability, we provide the solution process for (7) in the Appendix.

Let the solution to (7) be $\hat{\mathbf{M}}$, then the minimum number of non-panchromatic pixels will be $\|(\mathbf{C}\mathfrak{R}(\hat{\mathbf{M}}) + \mathbf{D}\mathfrak{I}(\hat{\mathbf{M}}))^T - \mathbf{1}/3\|_{2,0}$. The corresponding maximum percentage of panchromatic pixels is $1 - \|(\mathbf{C}\mathfrak{R}(\hat{\mathbf{M}}) + \mathbf{D}\mathfrak{I}(\hat{\mathbf{M}}))^T - \mathbf{1}/3\|_{2,0}/(n_r n_c)$. We discard the frequency structures whose maximum percentages of panchromatic pixels are below ρ , where ρ is a desired percentage of panchromatic pixels. As most of the existing high-sensitivity CFAs include 50% panchromatic pixels, we set

$\rho = 0.5$ in our experiments. We take the remaining frequency structures as candidates. So the minimum number of non-panchromatic pixels m_{\min} of every candidate is less than or equal to $\lfloor(1 - \rho)n_r n_c\rfloor$, where $\lfloor \cdot \rfloor$ denotes the floor function, which rounds a scalar to the largest integer less than or equal to that scalar.

B. Optimize Parameters

For every frequency structure candidate, $\lfloor(1 - \rho)n_r n_c\rfloor$ is in $[m_{\min}, +\infty)$, where m_{\min} is the minimum number of non-panchromatic pixels that it can produce. According to the analysis on the model problem in (6), every candidate is feasible to the following parameter optimization problem:

$$\begin{aligned} \min_{\mathbf{M}} & \|\mathbf{M}^{-1}\|_2 \\ \text{s.t. } & \mathbf{M}\mathbf{a} = \mathbf{b}, \mathbf{C}\mathfrak{R}(\mathbf{M}) + \mathbf{D}\mathfrak{I}(\mathbf{M}) \geq \mathbf{0}, \\ & \left\|(\mathbf{C}\mathfrak{R}(\mathbf{M}) + \mathbf{D}\mathfrak{I}(\mathbf{M}))^T - \mathbf{1}/3\right\|_{2,0} \leq \lfloor(1 - \rho)n_r n_c\rfloor. \end{aligned} \quad (8)$$

The solution to problem (8) results in a CFA whose percentage of panchromatic pixels is greater than or equal to ρ . Meanwhile, the robustness to aliasing artifacts of the CFA is maximized. So the obtained solution is an appropriately balanced solution to the multi-objective optimization problem (3). Due to the space limit, we move the details of solving (8) to the Supplementary Material.

IV. EXPERIMENTS

In this section, we conduct experiments on benchmark images to test the effectiveness of our high-sensitivity CFA design method. Our method consists of two sequential design steps, frequency structure selection and parameter optimization. So we first compare our parameter optimization method with those of other CFA design methods, where the first design step of our method is disabled and the frequency structures are given. Then we design a new CFA using the proposed method and compare it with other CFAs, where the two design steps are both active. The two comparisons together can testify to the effectiveness of both design steps.

A. Experimental Settings

1) *Compared Design Methods and CFAs*: We compare with five existing design methods for high-sensitivity CFAs. They are proposed by Compton and Hamilton, Jr., [6], Kumar *et al.* [7], Honda *et al.* [8], Wang *et al.* [9], and Chakrabarti *et al.* [10], respectively. We also compare with their designed CFAs on benchmark images. Since the Bayer CFA [5] is the most popular CFA in the literature, we also include it for comparison.

2) *Datasets*: We expect a CFA to work well in both low-light and normal-light conditions. So we evaluate the performance of CFAs on both low-light and normal-light datasets. It should be noted that, when capturing a normal-light scene, the panchromatic pixels are likely to be saturated due to their high light sensitivity. Following [27], we assume that the shutter speed of panchromatic pixels is controllable to users and the exposure times are carefully set so that the captured raw images have no saturated pixels.

We use the low-light dataset in [10], which is publicly available [32], to test the demosaicking performance in low-light conditions. It includes 10 images of indoor and outdoor scenes selected from the dataset of Gehler *et al.* [33]. These images are the linear version generated by Shi and Funt [34], where every 2×2 Bayer block in the original images is replaced with the average value of the block. All the 10 images are with a size of 2041×1359 pixels and encoded in RGB with 8 bits per channel.

We choose the commonly used Kodak dataset [11] as the normal-light dataset. It contains 24 images of various subjects in many locations. They are film captured and then digitized. The final images are padded to a size of 512×768 pixels and encoded in RGB with 8 bits per channel.

3) *Universal Demosaicking Algorithms*: We briefly introduce recent universal demosaicking algorithms, which are applicable to arbitrary periodic CFAs defined on the square lattice. Menon and Calvagno [35] proposed a regularization approach to demosaicking, which exploits global and local natural color image priors. Condat [36] presented a variational approach, where the reconstructed image has maximal smoothness under the constraint of being consistent with the measurements. Based on the spatio-spectral sampling theory and a filter-bank-based treatment of color image sampling, a nonlinear demosaicking algorithm was introduced by Gu *et al.* [37]. Singh and Singh [38] developed a demosaicking algorithm, which can be easily adapted to arbitrary CFAs. Based on the different frequency locations of luma and chromas of raw images captured by a periodic CFA, many frequency-selection-based demosaicking algorithms were proposed [14], [39], [40]. These algorithms are linear, which provides a good compromise between image quality and computational complexity.

In order to be fair, we adapt the least-squares luma-chroma demultiplexing (LSLCD) algorithm [40] to all the compared CFAs except the Chakrabarti CFA [10]. It is a frequency-selection-based demosaicking algorithm, where the filters are learned to minimize the mean-squared demosaicking error over a training image set. In all experiments, we use a 21×21 filter size. When testing a CFA on an image from a dataset, we learn

TABLE II

EVALUATION OF THE NUMERICAL STABILITY OF COLOR TRANSFORMATION. FOUR EXISTING DESIGN METHODS FOR HIGH-SENSITIVITY CFAS ARE COMPARED WITH THE PROPOSED ONE IN PARAMETER OPTIMIZATION. “ORIG.” STANDS FOR “ORIGINAL”. NOTE THAT OUR METHOD OBTAINS THE SAME $\|\mathbf{M}^\dagger\|_2$ VALUE BUT DIFFERENT \mathbf{M} AS THOSE OF THE HONDA CFA [8]. MOREOVER, OUR METHOD PRODUCES THE IDENTICAL \mathbf{M} AND HENCE THE SAME $\|\mathbf{M}^\dagger\|_2$ VALUE AS THOSE OF THE WANG CFA [9]

Numerical Stability	Compton [6] Orig.	Compton [6] Ours	Kumar [7] Orig.	Kumar [7] Ours	Honda [8] Orig.	Honda [8] Ours	Wang [9] Orig.	Wang [9] Ours
$\ \mathbf{M}^\dagger\ _2$	8	7.04	8	6.78	9.95	9.95	3.51	3.51

TABLE III

EVALUATION OF THE PROPOSED PARAMETER OPTIMIZATION METHOD ON THE LOW-LIGHT DATASET. “AVG.” STANDS FOR “AVERAGE”. THE INDIVIDUAL AND AVERAGE CPSNR VALUES ARE REPORTED. NOTE THAT OUR NEWLY DESIGNED CFA IS IDENTICAL TO THE WANG CFA [9]. SO THEIR CPSNR VALUES ARE THE SAME

Image ID	Compton [6]		Kumar [7]		Honda [8]		Wang [9]	
	Orig.	Ours	Orig.	Ours	Orig.	Ours	Orig.	Ours
01	41.07	41.85	41.09	41.95	41.43	41.77	41.95	41.95
02	40.17	40.75	40.19	40.87	40.60	40.78	41.02	41.02
03	38.63	39.56	38.55	39.74	39.16	39.52	39.78	39.78
04	42.80	44.13	42.89	44.20	42.89	43.61	44.04	44.04
05	47.08	47.65	47.10	47.56	47.17	47.27	47.53	47.53
06	34.98	36.06	35.00	36.22	35.64	35.54	36.85	36.85
07	36.58	37.50	36.58	37.66	37.14	37.03	37.92	37.92
08	42.02	42.76	42.03	42.72	42.39	42.36	42.62	42.62
09	43.26	44.29	43.28	44.23	43.63	43.56	44.24	44.24
10	40.12	41.76	40.15	41.77	40.55	40.83	41.71	41.71
Avg.	40.67	41.63	40.68	41.69	41.06	41.22	41.77	41.77

filters for the CFA on the remaining images of the dataset, resulting in a different set of filters for every test image. For example, when we attempt to test the Bayer CFA on an image from the Kodak dataset, we learn filters for this image on the other 23 images of the Kodak dataset. If a chroma of a CFA has multiple replicas, we simply average all estimations of the chroma. The Chakrabarti CFA has 15 different chromas (see Fig. 1(3f)), making the distances among chroma replicas very small (see Fig. 1(2f)). So the frequency-selection-based demosaicking is not appropriate for it. We use its associated reconstruction algorithm to demosaick it, whose source code is publicly available [32].

We note that *the demosaicking algorithms also affect the quality of demosaicked images. However, as we focus on designing CFAs, we do not conduct an extensive comparison of demosaicking algorithms in this work.*

B. Comparison of Parameter Optimization

For a given high-sensitivity CFA pattern, we can determine its number of panchromatic pixels, frequency structure, and color transformation matrix \mathbf{M} . However, for a given frequency structure and a feasible number of panchromatic pixels, we have to use a parameter optimization method to get an \mathbf{M} to finally obtain a high-sensitivity CFA pattern. This provides a chance to compare with other CFA design methods in parameter optimization.

For a high-sensitivity CFA pattern designed by an existing method, we first compute its frequency structure and the number of panchromatic pixels. Then with them, we obtain

TABLE IV

EVALUATION OF THE PROPOSED PARAMETER OPTIMIZATION METHOD ON THE KODAK DATASET. “AVG.” STANDS FOR “AVERAGE”. THE INDIVIDUAL AND AVERAGE CPSNR VALUES ARE REPORTED. NOTE THAT OUR NEWLY DESIGNED CFA IS IDENTICAL TO THE WANG CFA [9]. SO THEIR CPSNR VALUES ARE THE SAME

Image ID	Compton [6]		Kumar [7]		Honda [8]		Wang [9]	
	Orig.	Ours	Orig.	Ours	Orig.	Ours	Orig.	Ours
01	32.93	37.64	32.97	38.01	36.17	36.81	37.33	37.33
02	31.78	36.37	31.87	38.25	33.59	35.97	36.47	36.47
03	34.67	36.75	34.57	37.09	35.97	35.23	38.30	38.30
04	33.93	38.21	33.86	38.82	35.16	36.56	37.21	37.21
05	31.11	32.76	31.12	32.96	31.98	32.12	34.04	34.04
06	35.47	37.85	35.55	38.29	37.53	37.28	38.51	38.51
07	34.53	36.49	34.55	36.72	35.56	35.56	38.11	38.11
08	30.95	34.76	30.99	35.34	33.51	33.67	34.80	34.80
09	35.94	37.90	36.00	38.35	37.51	37.42	39.77	39.77
10	37.21	39.44	37.24	39.94	38.33	38.77	38.82	38.82
11	34.75	37.63	34.78	38.22	36.08	37.12	37.72	37.72
12	36.85	40.19	36.97	40.19	38.57	38.47	40.60	40.60
13	32.99	32.43	33.11	32.64	34.27	33.62	33.42	33.42
14	29.67	31.90	29.63	32.70	30.26	31.01	32.63	32.63
15	33.65	37.04	33.64	37.22	34.97	35.64	36.67	36.67
16	38.80	40.66	38.47	41.18	40.35	39.81	41.76	41.76
17	37.97	38.51	37.96	39.04	39.30	39.15	39.81	39.81
18	32.74	33.73	32.70	34.12	33.86	33.62	34.91	34.91
19	34.48	38.08	34.78	38.78	37.34	37.17	38.74	38.74
20	35.22	36.82	35.40	37.57	36.43	36.15	38.03	38.03
21	34.77	36.42	34.46	37.08	36.33	36.74	37.77	37.77
22	33.65	35.27	33.64	35.50	34.81	34.66	36.41	36.41
23	33.07	35.40	33.09	36.23	34.43	34.23	37.76	37.76
Avg.	34.16	36.49	34.17	37.01	35.66	35.84	37.24	37.24

TABLE V

EVALUATION OF THE PROPOSED Circ4 CFA ON THE LOW-LIGHT DATASET. SIX EXISTING CFAS ARE COMPARED WITH THE PROPOSED ONE, WHERE THE FIRST ROW ARE THEIR RESPECTIVE PERCENTAGES OF PANCHROMATIC PIXELS. THE INDIVIDUAL AND AVERAGE CPSNR VALUES ARE REPORTED

Image ID	0%	50%	50%	50%	40%	89%	50%
	Bayer [5]	Compton [6]	Kumar [7]	Honda [8]	Wang [9]	Chakrabarti [10]	Circ4
01	41.46	41.07	41.09	41.43	41.95	41.77	42.12
02	40.54	40.17	40.19	40.60	41.02	41.20	41.00
03	39.44	38.63	38.55	39.16	39.78	39.54	39.89
04	43.00	42.80	42.89	42.89	44.04	44.18	44.44
05	47.38	47.08	47.10	47.17	47.53	47.76	47.75
06	36.86	34.98	35.00	35.64	36.85	35.06	36.64
07	37.89	36.58	36.58	37.14	37.92	36.63	37.96
08	42.98	42.02	42.03	42.39	42.62	42.62	42.85
09	44.33	43.26	43.28	43.63	44.24	43.20	44.51
10	41.84	40.12	40.15	40.55	41.71	40.54	42.14
Avg.	41.57	40.67	40.68	41.06	41.77	41.25	41.93

a new \mathbf{M} as well as a new CFA by solving (8), where ρ is set to be the percentage of panchromatic pixels of the original CFA. We next compare the new CFA with the original one.

Since the newly designed CFA has an identical percentage of panchromatic pixels as the original one, we only compare the numerical stability of color transformation, which is related to the robustness to aliasing artifacts. We want to note that, in previous discussion, following most CFA design methods [12], [13], [15], [16], we assume that there are only two independent chromas in the frequency structures. Below Theorem 1 in the Appendix, we show that our parameter optimization model in (8) can be easily generalized to deal with frequency structures with more than two chromas. So for the general case, we compare $\|\mathbf{M}^\dagger\|_2$ instead of $\|\mathbf{M}^{-1}\|_2$. The values of $\|\mathbf{M}^\dagger\|_2$ are reported in Table II. A smaller value may

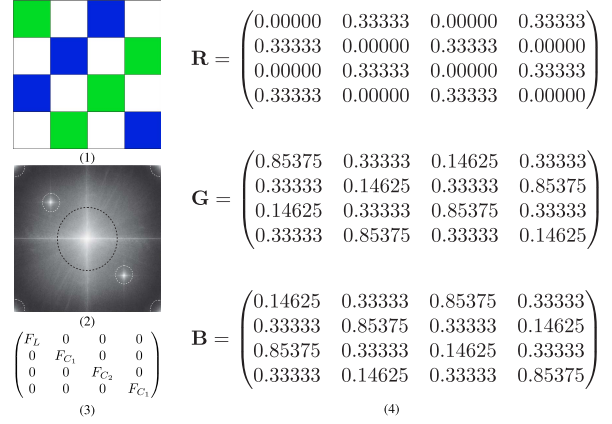


Fig. 4. The proposed Circ4 CFA pattern. (1) is the proposed 4×4 circulant CFA pattern. (2)-(4) are its spectrum, frequency structure, and color values, respectively. The notations in (2) and (3) are the same as those in Fig. 1.

TABLE VI

EVALUATION OF THE PROPOSED CIRC4 CFA ON THE KODAK DATASET. SIX EXISTING CFAS ARE COMPARED WITH THE PROPOSED ONE, WHERE THE FIRST ROW ARE THEIR RESPECTIVE PERCENTAGES OF PANCHROMATIC PIXELS. THE INDIVIDUAL AND AVERAGE CPSNR VALUES ARE REPORTED

Image ID	0%	50%	50%	50%	40%	89%	50%
	Bayer [5]	Compton [6]	Kumar [7]	Honda [8]	Wang [9]	Chakrabarti [10]	Circ4
01	37.35	32.93	32.97	36.17	37.33	31.72	39.17
02	36.49	31.78	31.87	33.59	36.47	30.97	39.31
03	39.31	34.67	34.57	35.97	38.30	36.23	37.83
04	38.32	33.93	33.86	35.16	37.21	33.33	39.88
05	35.80	31.11	31.12	31.98	34.04	29.93	33.93
06	37.95	35.47	35.55	37.53	38.51	33.40	39.33
07	39.30	34.53	34.55	35.56	38.11	34.28	37.51
08	33.53	30.95	30.99	33.51	34.80	30.42	36.36
09	40.20	35.94	36.00	37.51	39.77	37.75	39.19
10	40.50	37.21	37.24	38.33	38.82	36.76	40.71
11	38.42	34.75	34.78	36.08	37.72	33.12	39.29
12	40.79	36.85	36.97	38.57	40.60	37.53	41.03
13	35.37	32.99	33.11	34.27	33.42	28.60	33.70
14	33.51	29.67	29.63	30.26	32.63	30.71	33.36
15	36.89	33.65	33.64	34.97	36.67	34.49	38.11
16	40.41	38.80	38.47	40.35	41.76	36.33	42.24
17	40.38	37.97	37.96	39.30	39.81	36.31	39.92
18	36.03	32.74	32.70	33.86	34.91	30.74	34.92
19	37.99	34.48	34.78	37.34	38.74	34.29	39.46
20	38.36	35.22	35.40	36.43	38.03	35.41	38.30
21	37.54	34.77	34.46	36.33	37.77	33.41	38.23
22	36.89	33.65	33.64	34.81	36.41	33.08	36.58
23	38.44	33.07	33.09	34.43	37.76	35.73	37.17
24	34.68	32.73	32.75	33.48	34.07	30.34	34.84
Avg.	37.69	34.16	34.17	35.66	37.24	33.54	37.93

indicate higher numerical stability and hence more robustness to aliasing artifacts. From left to right, the four groups of comparisons correspond to the Compton CFA [6], Kumar CFA [7], Honda CFA [8], and Wang CFA [9], respectively. Note that the $\|\mathbf{M}^\dagger\|_2$ values cannot be directly compared across different CFAs [12], [13]. We can see that our new color transformations based on the Compton CFA and the Kumar CFA are more stable than those of the original ones (see the first two groups of Table II). Our method obtains the identical $\|\mathbf{M}^\dagger\|_2$ value but different \mathbf{M} as those of the Honda CFA (see the third group of Table II). It seems to show that the Honda CFA is comparable to our newly designed one.

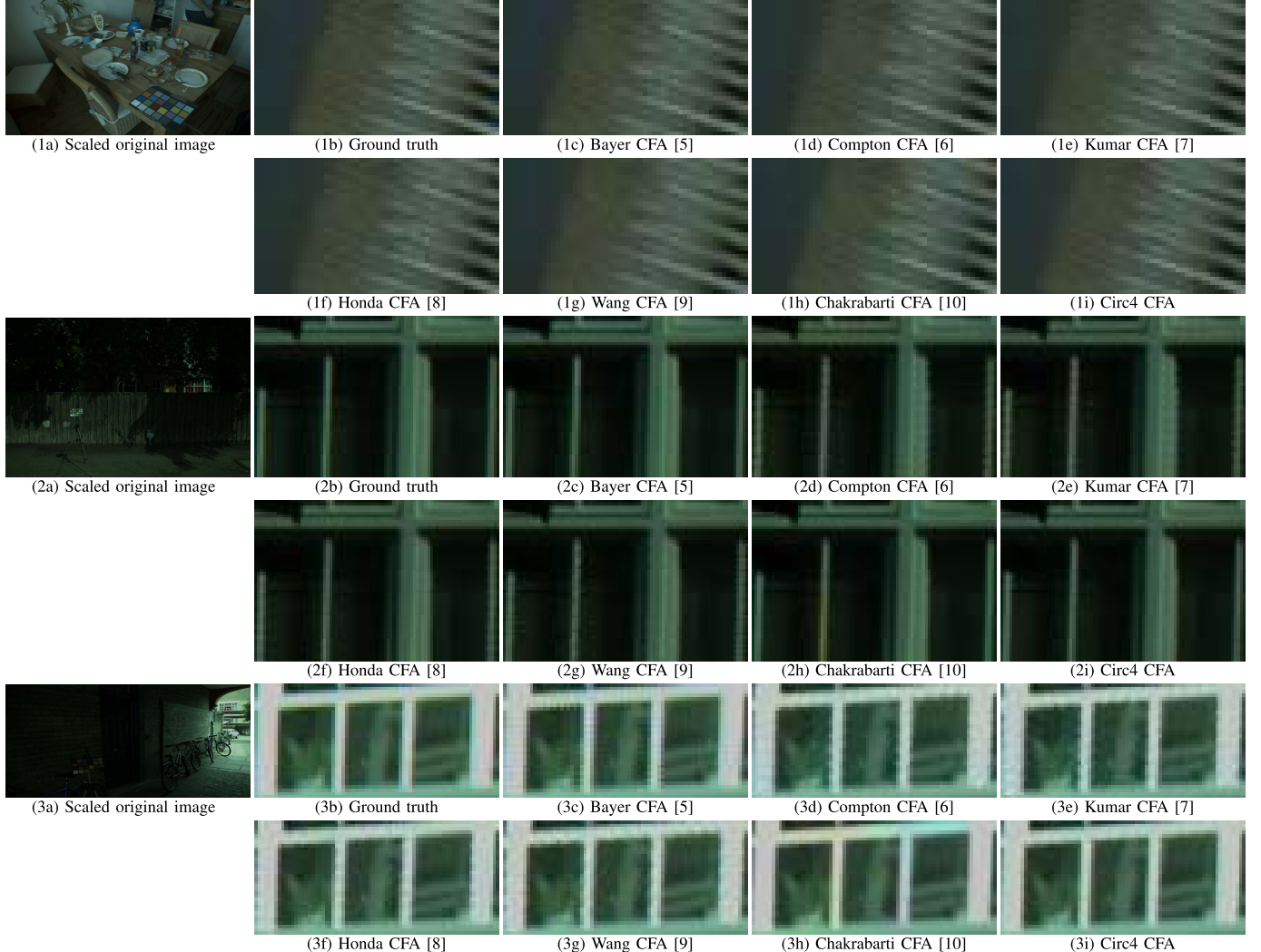


Fig. 5. Blowups of some demosaicked images in the low-light dataset. From top to bottom, the images are from #3, #9, and #10 images of the low-light dataset, respectively. In each group, (a) is the scaled original image, in which the red rectangle indicates the selected patch to blow up; (b) is the ground truth; (c)-(h) and (i) are the images demosaicked from the raw images by other CFAs and the proposed one, respectively. From all the groups of images, we can clearly see that there are obvious zipper effects or false color artifacts along edges in the images demosaicked from the raw images by other CFAs, while those by our Circ4 CFA have better visual quality.

However, the following comparisons show that the new CFA still outperforms the original one. Our method produces an identical \mathbf{M} as that of the Wang CFA, which implies that the parameters of the Wang CFA are already optimal for its frequency structure with its number of panchromatic pixels. So the $\|\mathbf{M}^\dagger\|_2$ values are also the same.

Then with the same demosaicking algorithm, we compare the newly designed CFAs with their respective original ones on both low-light and Kodak datasets. The CPSNR values are reported in Table III and Table IV, respectively. The better values in each group are in boldface. Concurring the comparisons on $\|\mathbf{M}^\dagger\|_2$, our newly designed CFAs outperform the Compton CFA and the Kumar CFA with significant gaps on both low-light and Kodak datasets (see the first two groups of Table III and Table IV). Our new CFA designed according to the Honda CFA slightly outperforms the original one on both datasets (see the third groups of Table III and Table IV). As our new CFA designed according to the Wang CFA is identical to

the original one, they have the same CPSNR values (see the last groups of Table III and Table IV).

C. Comparison of CFAs

We first generate a new CFA pattern using our design method and then compare it with the others on both low-light and Kodak datasets. The design process for a given CFA pattern size is demonstrated in Fig. 3. We check all pattern sizes that are smaller than or equal to 9×9 . The CFA pattern that performs the best in our tests is shown in Fig. 4. It is a 4×4 CFA pattern with 50% panchromatic pixels (Fig. 4(1)). Also, it is clear that *the new CFA pattern has only two color components, making its manufacturing much more advantageous*. Our CFA pattern is circulant, so we call it the Circ4 CFA pattern. Its spectrum and frequency structure are shown in Fig. 4(2) and 4(3), respectively. We can see that all its chroma replicas are located far away from the center and the horizontal and the vertical axes. The color values of

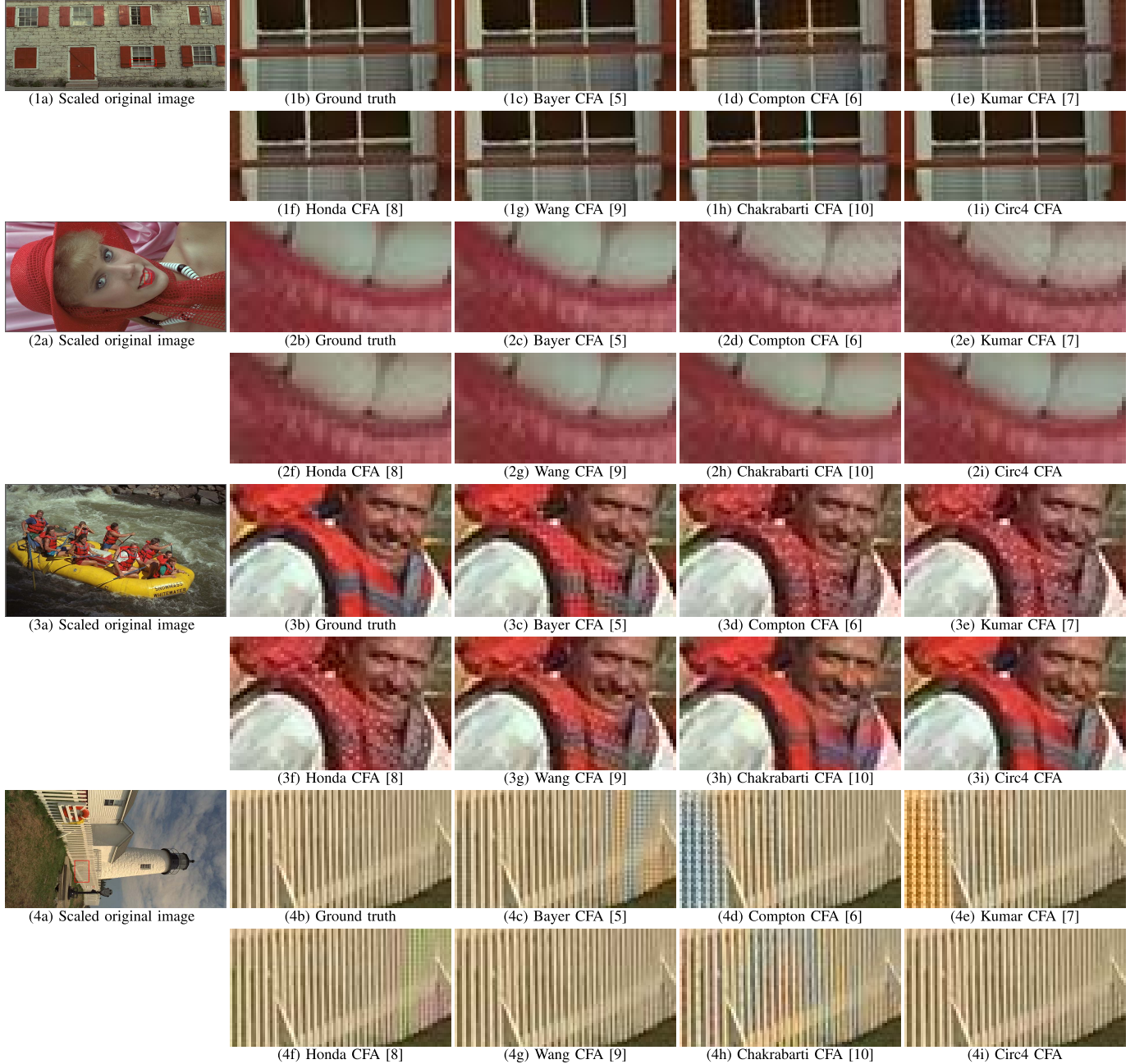


Fig. 6. Blowups of some demosaicked images in the Kodak dataset. From top to bottom, the images are from #1, #4, #14, and #19 images of the Kodak dataset, respectively. In each group, (a) is the scaled original image, in which the red rectangle indicates the selected patch to blow up; (b) is the ground truth; (c)-(h) and (i) are the images demosaicked from the raw images by other CFAs and the proposed one, respectively. From all groups of images, we can clearly see that the images demosaicked from the raw images with other CFAs have severe zipper effects or false color artifacts, while those by our Circ4 CFA have better subjective quality. We want to note that, in the last group, the images by the Wang CFA and Circ4 CFA are almost perfect, which testifies to the importance of reducing spectral overlap for suppressing aliasing artifacts.

the Circ4 CFA pattern are shown in Fig. 4(4), while its color transformation matrix \mathbf{M} is:

$$\mathbf{M} = \begin{pmatrix} 0.16666 & 0.41667 & 0.41667 \\ 0.00000 & 0.17688 & -0.17688 \\ -0.16666 & 0.08333 & 0.08333 \end{pmatrix}.$$

Then we test the demosaicking performance of our new CFA on both low-light and Kodak datasets. The CPSNR values on the two datasets are reported in Table V and Table VI, respectively. The best values are in boldface. As mentioned

before, we use the associated reconstruction algorithm for the Chakrabarti CFA [10] and the modified LSLCD algorithm [40] for other CFAs. Besides the existing high-sensitivity CFAs, we also include the Bayer CFA for comparison. The CFAs with different percentages of panchromatic pixels are compared separately. With the identical percentage of panchromatic pixels, we can see that our Circ4 CFA significantly outperforms the Compton CFA, Kumar CFA, and Honda CFA on both low-light and Kodak datasets with gaps of about 1dB and 3dB in average, respectively. The Bayer CFA and

Wang CFA have lower percentages of panchromatic pixels than our Circ4 CFA does, which implies that they are inferior in light sensitivity. Besides that, the Circ4 CFA also results in better CPSNR values on both low-light and Kodak datasets. The Chakrabarti CFA includes a higher percentage of panchromatic pixels than the Circ4 CFA does. Benefiting from this as well as the associated reconstruction algorithm, it also achieves competitive CPSNR values on the low-light dataset, which is inferior to our Circ4 CFA with a gap of 0.68dB in average. However, when compared on the Kodak dataset, the Chakrabarti CFA is much worse than the Circ4 CFA with a significant gap of 4.39dB in average. Thus we consider that the Chakrabarti CFA values light sensitivity more than color fidelity, which can be further verified in the following visual comparison.

We also present part of the visual comparison on the low-light and Kodak datasets in Fig. 5 and Fig. 6, respectively. We can see that the visual quality of our Circ4 CFA is better than the others on both datasets (Please read the captions for the descriptions on visual difference.).

V. CONCLUSIONS

In this paper, we have extended the approach in [13] to design high-sensitivity CFAs with panchromatic pixels in the frequency domain, which has a mathematical model and is fully automatic. To accomplish this, we formulated high-sensitivity CFA design with panchromatic pixels as a multi-objective optimization problem, which simultaneously maximizes the robustness to aliasing artifacts and the percentage of panchromatic pixels. We analyzed the new formulation, based on which we proposed a new high-sensitivity CFA design method. Extensive experiments on both low-light and normal-light datasets have demonstrated the superiority of our design method. Future work will include adapting our method to design various specific CFAs such as for given demosaicking algorithms and specialized cameras.

APPENDIX SOLVING PROBLEM (7)

We use the alternating direction method (ADM) [41] to solve problem (7). Since ADM requires linear constraints, we first let $\mathbf{C} = \mathbf{C}_1 + i\mathbf{C}_2$ and $\mathbf{D} = \mathbf{D}_1 + i\mathbf{D}_2$, then the constraint $\mathbf{C}\Re(\mathbf{M}) + \mathbf{D}\Im(\mathbf{M}) \geq \mathbf{0}$ in (7) can be written into two linear ones: $\mathbf{C}_1\Re(\mathbf{M}) + \mathbf{D}_1\Im(\mathbf{M}) \geq \mathbf{0}$ and $\mathbf{C}_2\Re(\mathbf{M}) + \mathbf{D}_2\Im(\mathbf{M}) = \mathbf{0}$. So we rewrite (7) as follows:

$$\begin{aligned} & \min_{\mathbf{M}} \left\| (\mathbf{C}_1\Re(\mathbf{M}) + \mathbf{D}_1\Im(\mathbf{M}))^T - \mathbf{1}/3 \right\|_{2,0} \\ & \text{s.t. } \mathbf{M}\mathbf{a} = \mathbf{b}, \mathbf{C}_1\Re(\mathbf{M}) + \mathbf{D}_1\Im(\mathbf{M}) \geq \mathbf{0}, \\ & \quad \|\mathbf{M}^{-1}\|_2 \leq \nu, \mathbf{C}_2\Re(\mathbf{M}) + \mathbf{D}_2\Im(\mathbf{M}) = \mathbf{0}. \end{aligned} \quad (9)$$

We next introduce three auxiliary variables \mathbf{N}_1 , \mathbf{N}_2 , and \mathbf{S} to reformulate (9) as follows:

$$\begin{aligned} & \min_{\mathbf{M}, \mathbf{N}_1, \mathbf{N}_2, \mathbf{S}} \mathcal{I}_{\Phi}(\mathbf{M}) + \mathcal{I}_{\Psi}(\mathbf{S}) + \|\mathbf{S}\|_{2,0} \\ & \text{s.t. } \mathbf{M} = \mathbf{N}_1 + i\mathbf{N}_2, (\mathbf{N}_1 + i\mathbf{N}_2)\mathbf{a} = \mathbf{b}, \\ & \quad (\mathbf{C}_1\mathbf{N}_1 + \mathbf{D}_1\mathbf{N}_2)^T - \mathbf{1}/3 = \mathbf{S}, \mathbf{C}_2\mathbf{N}_1 + \mathbf{D}_2\mathbf{N}_2 = \mathbf{0}, \end{aligned} \quad (10)$$

where $\Phi = \{\mathbf{M} \mid \|\mathbf{M}^{-1}\|_2 \leq \nu\}$, $\Psi = \{\mathbf{S} \mid \mathbf{S} \geq -\mathbf{1}/3\}$, and $\mathcal{I}_{\Phi}(\cdot)$ and $\mathcal{I}_{\Psi}(\cdot)$ are indicator functions defined on Φ and Ψ , respectively. The indicator function of a set Γ is defined as

$$\mathcal{I}_{\Gamma}(\mathbf{y}) = \begin{cases} 0, & \mathbf{y} \in \Gamma, \\ +\infty, & \text{otherwise.} \end{cases}$$

The augmented Lagrangian function of problem (10) is:

$$\begin{aligned} \mathcal{L}(\mathbf{M}, \mathbf{N}_1, \mathbf{N}_2, \mathbf{S}, \mathbf{X}, \mathbf{x}, \mathbf{Y}, \mathbf{Z}) &= \mathcal{I}_{\Phi}(\mathbf{M}) + \mathcal{I}_{\Psi}(\mathbf{S}) + \|\mathbf{S}\|_{2,0} \\ &+ \langle \mathbf{X}, \mathbf{M} - (\mathbf{N}_1 + i\mathbf{N}_2) \rangle + \langle \mathbf{x}, (\mathbf{N}_1 + i\mathbf{N}_2)\mathbf{a} - \mathbf{b} \rangle \\ &+ \langle \mathbf{Y}, (\mathbf{C}_1\mathbf{N}_1 + \mathbf{D}_1\mathbf{N}_2)^T - \mathbf{1}/3 - \mathbf{S} \rangle + \langle \mathbf{Z}, \mathbf{C}_2\mathbf{N}_1 + \mathbf{D}_2\mathbf{N}_2 \rangle \\ &+ \frac{\beta}{2} \left(\|\mathbf{M} - (\mathbf{N}_1 + i\mathbf{N}_2)\|_F^2 + \|(\mathbf{N}_1 + i\mathbf{N}_2)\mathbf{a} - \mathbf{b}\|_2^2 \right. \\ &\left. + \|(\mathbf{C}_1\mathbf{N}_1 + \mathbf{D}_1\mathbf{N}_2)^T - \mathbf{1}/3 - \mathbf{S}\|_F^2 + \|\mathbf{C}_2\mathbf{N}_1 + \mathbf{D}_2\mathbf{N}_2\|_F^2 \right), \end{aligned} \quad (11)$$

where \mathbf{X} , \mathbf{x} , \mathbf{Y} , and \mathbf{Z} are the Lagrange multipliers, $\langle \cdot, \cdot \rangle$ is the inner product, and $\beta > 0$ is the penalty parameter which is updated during iterations.

Then by ADM, we can solve problem (10) via the following iterations:

$$\begin{aligned} \mathbf{M}^{k+1} &= \operatorname{argmin}_{\mathbf{M}} \mathcal{L}(\mathbf{M}, \mathbf{N}_1^k, \mathbf{N}_2^k, \mathbf{S}^k, \mathbf{X}^k, \mathbf{x}^k, \mathbf{Y}^k, \mathbf{Z}^k) \\ &= \operatorname{argmin}_{\mathbf{M}} \mathcal{I}_{\Phi}(\mathbf{M}) + \frac{\beta}{2} \|\mathbf{M} - (\mathbf{N}_1^k + i\mathbf{N}_2^k) + \mathbf{X}^k/\beta\|_F^2 \\ &= \operatorname{argmin}_{\mathbf{M}} \mathcal{I}_{\Phi}(\mathbf{M}) + \frac{1}{2} \|\mathbf{M} - \mathbf{W}^k\|_F^2, \end{aligned} \quad (12)$$

$$\begin{aligned} \{\mathbf{N}_j^{k+1}\}_{j=1}^2 &= \operatorname{argmin}_{\mathbf{N}_1, \mathbf{N}_2} \mathcal{L}(\mathbf{M}^{k+1}, \mathbf{N}_1, \mathbf{N}_2, \mathbf{S}^k, \mathbf{X}^k, \mathbf{x}^k, \mathbf{Y}^k, \mathbf{Z}^k) \\ &= \operatorname{argmin}_{\mathbf{N}_1, \mathbf{N}_2} \frac{1}{2} \|\mathbf{M}^{k+1} - (\mathbf{N}_1 + i\mathbf{N}_2) + \mathbf{X}^k/\beta\|_F^2 \\ &\quad + \frac{1}{2} \|(\mathbf{N}_1 + i\mathbf{N}_2)\mathbf{a} - \mathbf{b} + \mathbf{x}^k/\beta\|_2^2 \\ &\quad + \frac{1}{2} \|\mathbf{C}_1\mathbf{N}_1 + \mathbf{D}_1\mathbf{N}_2 - (\mathbf{1}/3 + \mathbf{S}^k - \mathbf{Y}^k/\beta)^T\|_F^2 \\ &\quad + \frac{1}{2} \|\mathbf{C}_2\mathbf{N}_1 + \mathbf{D}_2\mathbf{N}_2 + \mathbf{Z}^k/\beta\|_F^2, \end{aligned} \quad (13)$$

$$\begin{aligned} \mathbf{S}^{k+1} &= \operatorname{argmin}_{\mathbf{S}} \mathcal{L}(\mathbf{M}^{k+1}, \mathbf{N}_1^{k+1}, \mathbf{N}_2^{k+1}, \mathbf{S}, \mathbf{X}^k, \mathbf{x}^k, \mathbf{Y}^k, \mathbf{Z}^k) \\ &= \operatorname{argmin}_{\mathbf{S}} \mathcal{I}_{\Psi}(\mathbf{S}) + \|\mathbf{S}\|_{2,0} \\ &\quad + \frac{\beta}{2} \|(\mathbf{C}_1\mathbf{N}_1^{k+1} + \mathbf{D}_1\mathbf{N}_2^{k+1})^T - \mathbf{1}/3 - \mathbf{S} + \mathbf{Y}^k/\beta\|_F^2 \\ &= \operatorname{argmin}_{\mathbf{S}} \mathcal{I}_{\Psi}(\mathbf{S}) + \|\mathbf{S}\|_{2,0} + \frac{\beta}{2} \|\mathbf{S} - \mathbf{P}^k\|_F^2 \\ &= \max(-\mathbf{1}/3, \operatorname{prox}_{2/\beta}^{\ell_{2,0}}(\mathcal{R}(\mathbf{P}^k))), \end{aligned} \quad (14)$$

$$\mathbf{X}^{k+1} = \mathbf{X}^k + \beta(\mathbf{M}^{k+1} - (\mathbf{N}_1^{k+1} + i\mathbf{N}_2^{k+1})), \quad (15)$$

$$\mathbf{x}^{k+1} = \mathbf{x}^k + \beta((\mathbf{N}_1^{k+1} + i\mathbf{N}_2^{k+1})\mathbf{a} - \mathbf{b}), \quad (16)$$

$$\mathbf{Y}^{k+1} = \mathbf{Y}^k + \beta((\mathbf{C}_1\mathbf{N}_1^{k+1} + \mathbf{D}_1\mathbf{N}_2^{k+1})^T - \mathbf{1}/3 - \mathbf{S}^{k+1}), \quad (17)$$

$$\mathbf{Z}^{k+1} = \mathbf{Z}^k + \beta(\mathbf{C}_2\mathbf{N}_1^{k+1} + \mathbf{D}_2\mathbf{N}_2^{k+1}), \quad (18)$$

where $\mathbf{W}^k = (\mathbf{N}_1^k + i\mathbf{N}_2^k) - \mathbf{X}^k/\beta$ in (13), $\mathbf{P}^k = (\mathbf{C}_1\mathbf{N}_1^{k+1} + \mathbf{D}_1\mathbf{N}_2^{k+1})^T - \mathbf{1}/3 + \mathbf{Y}^k/\beta$ in (14), and $\text{prox}_{\psi}^{\ell_{2,0}}(\cdot)$ is the proximal operator of $\ell_{2,0}$ -norm for a positive constant ψ , which is defined by

$$\text{prox}_{\psi}^{\ell_{2,0}}(\mathbf{H}) = \underset{\mathbf{J}}{\operatorname{argmin}} \psi \|\mathbf{J}\|_{2,0} + \|\mathbf{J} - \mathbf{H}\|_F^2. \quad (19)$$

The j -th column of $\text{prox}_{\psi}^{\ell_{2,0}}(\mathbf{H})$ is computed as:

$$[\text{prox}_{\psi}^{\ell_{2,0}}(\mathbf{H})]_{:,j} = \begin{cases} [\mathbf{H}]_{:,j}, & \text{if } \|[\mathbf{H}]_{:,j}\|_2^2 > \psi, \\ \mathbf{0}, & \text{otherwise.} \end{cases}$$

The solution to problem (13) is given by Theorem 1, whose proof can be found in the Supplementary Material.

Theorem 1: The solution to problem (12) is:

$$\mathbf{M}^{k+1} = \mathbf{U}^k \Sigma^{k+1} (\mathbf{V}^k)^H, \quad (20)$$

where $\mathbf{U}^k \Lambda^k (\mathbf{V}^k)^H$ is the full SVD of \mathbf{W}^k , \mathbf{U}^k and \mathbf{V}^k are unitary matrices, $\Lambda^k = \text{diag}(\boldsymbol{\lambda}^k)$, $\boldsymbol{\lambda}^k = (\lambda_1^k, \lambda_2^k, \lambda_3^k)^T$ is the vector of singular values of \mathbf{W}^k and satisfies $\lambda_1^k \geq \lambda_2^k \geq \lambda_3^k > 0$, and $\Sigma^{k+1} = \text{diag}(\boldsymbol{\sigma}^{k+1})$, in which $\boldsymbol{\sigma}^{k+1} = (\sigma_1^{k+1}, \sigma_2^{k+1}, \sigma_3^{k+1})^T$ is defined as:

$$\boldsymbol{\sigma}^{k+1} = \max(1/\nu, \boldsymbol{\lambda}^k). \quad (21)$$

It should be noted that, in the above theorem as well as the model in (7), \mathbf{M} is assumed to be a 3×3 invertible matrix. This implies that the frequency structure has only one luma and two independent chromas. However, $\mathbf{M} \in \mathbb{C}^{n \times 3}$ is of full column rank in general, where $n \geq 3$ is the number of frequency components. In this case, we only need to replace the full SVD and \mathbf{M}^{-1} with the skinny SVD and \mathbf{M}^\dagger , respectively. Other than that there are no changes in Theorem 1 and the whole solution process of problem (7). Note that for a full column rank matrix $\mathbf{M} \in \mathbb{C}^{n \times 3}$, its full SVD is defined by $(\mathbf{U}_1, \mathbf{U}_2)(\Sigma^T, \mathbf{0}^T)^T \mathbf{V}^H$, where $(\mathbf{U}_1, \mathbf{U}_2) \in \mathbb{C}^{n \times n}$ and $\mathbf{V} \in \mathbb{C}^{3 \times 3}$ are both unitary matrices, $\mathbf{U}_1 \in \mathbb{C}^{n \times 3}$, and $\Sigma \in \mathbb{R}^{3 \times 3}$ is a diagonal matrix, whose diagonal elements are the positive singular values of \mathbf{M} . However, its skinny SVD is defined as $\mathbf{U}_1 \Sigma \mathbf{V}^H$.

Problem (13) has a closed-form solution and we show the solution process as follows. Let $\mathbf{E} = \begin{pmatrix} \mathbf{N}_1 \\ \mathbf{N}_2 \end{pmatrix}$ in (13), then the objective function of (13) becomes:

$$\begin{aligned} \mathcal{F}(\mathbf{E}) = & \frac{1}{2} \left\| \mathbf{M}^{k+1} - (\mathbf{I}, i\mathbf{I})\mathbf{E} + \mathbf{X}^k/\beta \right\|_F^2 \\ & + \frac{1}{2} \left\| (\mathbf{I}, i\mathbf{I})\mathbf{E} - \mathbf{b} + \mathbf{x}^k/\beta \right\|_2^2 \\ & + \frac{1}{2} \left\| (\mathbf{C}_1, \mathbf{D}_1)\mathbf{E} - (\mathbf{1}/3 + \mathbf{S}^k - \mathbf{Y}^k/\beta)^T \right\|_F^2 \\ & + \frac{1}{2} \left\| (\mathbf{C}_2, \mathbf{D}_2)\mathbf{E} + \mathbf{Z}^k/\beta \right\|_F^2. \end{aligned} \quad (22)$$

It is equivalent to the following function:

$$\begin{aligned} f(\text{vec}(\mathbf{E})) = & \frac{1}{2} \|\mathbf{A}_1 \text{vec}(\mathbf{E}) - \mathbf{b}_1^k\|_2^2 + \frac{1}{2} \|\mathbf{A}_2 \text{vec}(\mathbf{E}) - \mathbf{b}_2^k\|_2^2 \\ & + \frac{1}{2} \|\mathbf{A}_3 \text{vec}(\mathbf{E}) - \mathbf{b}_3^k\|_2^2 + \frac{1}{2} \|\mathbf{A}_4 \text{vec}(\mathbf{E}) - \mathbf{b}_4^k\|_2^2, \end{aligned} \quad (23)$$

Algorithm 1 The ADM Algorithm for Problem (9)

Input: $\mathbf{C}, \mathbf{D}, \mathbf{a}, \mathbf{b}, \nu = 100, m_{\min} = n_r n_c, \beta = 1, \beta_{\max} = 10^4, \gamma = 1.1, \varepsilon_1 = 10^{-8}$, and $\varepsilon_2 = 10^{-8}$.

- 1: **for** each \mathbf{N}_1 and $\mathbf{N}_2 \in \Omega$ defined in (28) **do**
- 2: **Initialization:** $\mathbf{S} = (\mathbf{C}_1\mathbf{N}_1 + \mathbf{D}_1\mathbf{N}_2)^T - \mathbf{1}/3, \mathbf{X} = \mathbf{0}, \mathbf{x} = \mathbf{0}, \mathbf{Y} = \mathbf{0}, \mathbf{Z} = \mathbf{0}, k = 0$.
- 3: **while** the stop conditions (26) and (27) are not met **do**
- 4: fix the others and update \mathbf{M} by (20).
- 5: fix the others and update \mathbf{N}_1 and \mathbf{N}_2 by (24).
- 6: fix the others and update \mathbf{S} by (14).
- 7: update the multipliers $\mathbf{X}, \mathbf{x}, \mathbf{Y}$, and \mathbf{Z} by (15)-(18).
- 8: update β by (25).
- 9: $k \leftarrow k + 1$.
- 10: **end while**
- 11: compute $\hat{m} = \|(\mathbf{C}_1\Re(\mathbf{M}) + \mathbf{D}_1\Im(\mathbf{M}))^T - \mathbf{1}/3\|_{2,0}$.
- 12: **if** $\hat{m} < m_{\min}$ **then**
- 13: $m_{\min} \leftarrow \hat{m}$.
- 14: **end if**
- 15: **end for**

Output: m_{\min} .

where $\mathbf{A}_1 = \mathbf{I} \otimes (\mathbf{I}, i\mathbf{I}), \mathbf{A}_2 = \mathbf{a}^T \otimes (\mathbf{I}, i\mathbf{I}), \mathbf{A}_3 = \mathbf{I} \otimes (\mathbf{C}_1, \mathbf{D}_1), \mathbf{A}_4 = \mathbf{I} \otimes (\mathbf{C}_2, \mathbf{D}_2), \mathbf{b}_1^k = \mathbf{A}_1^H \text{vec}(\mathbf{M}^{k+1} + \mathbf{X}^k/\beta), \mathbf{b}_2^k = \mathbf{A}_2^H (\mathbf{b} - \mathbf{x}^k/\beta), \mathbf{b}_3^k = \mathbf{A}_3^H \text{vec}((\mathbf{1}/3 + \mathbf{S}^k - \mathbf{Y}^k/\beta)^T), \mathbf{b}_4^k = \mathbf{A}_4^H \text{vec}(-\mathbf{Z}^k/\beta)$, \otimes denotes the Kronecker product, and \mathbf{I} is a 3×3 ($n \times n$ for the general case) identity matrix. Setting $\frac{\partial f}{\partial \text{vec}(\mathbf{E})} = 0$, we have the solution to (23) as follows:

$$\text{vec}(\mathbf{E}^{k+1}) = \text{vec} \begin{pmatrix} \mathbf{N}_1^{k+1} \\ \mathbf{N}_2^{k+1} \end{pmatrix} = \mathbf{G}^{-1} (\mathbf{b}_1^k + \mathbf{b}_2^k + \mathbf{b}_3^k + \mathbf{b}_4^k), \quad (24)$$

where $\mathbf{G} = \mathbf{A}_1^H \mathbf{A}_1 + \mathbf{A}_2^H \mathbf{A}_2 + \mathbf{A}_3^H \mathbf{A}_3 + \mathbf{A}_4^H \mathbf{A}_4$.

To accelerate convergence, we use the following strategy to adaptively update the penalty parameter β [41]:

$$\beta^{k+1} = \begin{cases} \min(\beta_{\max}, \beta^k \gamma), & \text{if } \beta^k \alpha^k < \varepsilon_1, \\ \beta^k, & \text{otherwise,} \end{cases} \quad (25)$$

where β_{\max} is an upper bound of $\{\beta^k\}$, $\gamma \geq 1$ is a constant and $\alpha^k = \max\{\|\mathbf{M}^{k+1} - \mathbf{M}^k\|_\infty, \|\mathbf{N}_1^{k+1} - \mathbf{N}_1^k\|_\infty, \|\mathbf{N}_2^{k+1} - \mathbf{N}_2^k\|_\infty, \|\mathbf{S}^{k+1} - \mathbf{S}^k\|_\infty\}$. The stopping criteria are:

$$\beta^k \alpha^k < \varepsilon_1 \quad \text{and} \quad (26)$$

$$\begin{aligned} & \max\{\|\mathbf{M}^{k+1} - \mathbf{N}_1^{k+1} - i\mathbf{N}_2^{k+1}\|_\infty, \\ & \quad \|(\mathbf{N}_1^{k+1} + i\mathbf{N}_2^{k+1})\mathbf{a} - \mathbf{b}\|_\infty, \\ & \quad \|(\mathbf{C}_1\mathbf{N}_1^{k+1} + \mathbf{D}_1\mathbf{N}_2^{k+1})^T - \mathbf{1}/3 - \mathbf{S}^{k+1}\|_\infty, \\ & \quad \|\mathbf{C}_2\mathbf{N}_1^{k+1} + \mathbf{D}_2\mathbf{N}_2^{k+1}\|_\infty\} < \varepsilon_2. \end{aligned} \quad (27)$$

Since problem (9) is non-convex, different initializations of \mathbf{M} may lead to different local minima. As in [13], we initialize \mathbf{M} with every element in the following set and finally select the \mathbf{M} that resulted in the smallest number of non-panchromatic

pixels:

$$\Omega = \{\text{diag}((1, 1, 1)^T), \text{diag}((1, 1, -1)^T), \text{diag}((1, -1, 1)^T), \\ \text{diag}((1, -1, -1)^T), \text{diag}((-1, 1, 1)^T), \\ \text{diag}((-1, 1, -1)^T), \\ \text{diag}((-1, -1, 1)^T), \text{diag}((-1, -1, -1)^T)\}. \quad (28)$$

We summarize the whole solution process of problem (9) in Algorithm 1.

REFERENCES

- [1] B. K. Gunturk, J. Glotzbach, Y. Altunbasak, R. W. Schafer, and R. M. Mersereau, "Demosaicing: Color filter array interpolation," *IEEE Signal Process. Mag.*, vol. 22, no. 1, pp. 44–54, Jan. 2005.
- [2] X. Li, B. Gunturk, and L. Zhang, "Image demosaicing: A systematic survey," *Proc. SPIE*, vol. 6822, p. 68221J, Jan. 2008.
- [3] D. Menon and G. Calvagno, "Color image demosaicing: An overview," *Signal Process., Image Commun.*, vol. 26, nos. 8–9, pp. 518–533, Oct. 2011.
- [4] C. Bai, J. Li, Z. Lin, J. Yu, and Y.-W. Chen, "Penrose demosaicing," *IEEE Trans. Image Process.*, vol. 24, no. 5, pp. 1672–1684, May 2015.
- [5] B. E. Bayer, "Color imaging array," U.S. Patent 3971065, Jul. 20, 1976.
- [6] J. T. Compton and J. F. Hamilton, Jr., "Image sensor with improved light sensitivity," U.S. Patent 20070024931, Feb. 1, 2007.
- [7] M. Kumar, E. O. Morales, J. E. Adams, Jr., and W. Hao, "New digital camera sensor architecture for low light imaging," in *Proc. IEEE Int. Conf. Image Process.*, Nov. 2009, pp. 2681–2684.
- [8] H. Honda, Y. Iida, Y. Egawa, and H. Seki, "A color CMOS imager with 4×4 white-RGB color filter array for increased low-illumination signal-to-noise ratio," *IEEE Trans. Electron Devices*, vol. 56, no. 11, pp. 2398–2402, Nov. 2009.
- [9] J. Wang, C. Zhang, and P. Hao, "New color filter arrays of high light sensitivity and high demosaicing performance," in *Proc. IEEE Int. Conf. Image Process.*, Sep. 2011, pp. 3153–3156.
- [10] A. Chakrabarti, W. T. Freeman, and T. Zickler, "Rethinking color cameras," in *Proc. IEEE Int. Conf. Comput. Photogr.*, May 2014, pp. 1–8.
- [11] (Dec. 1, 2013), *Kodak Lossless True Color Image Suite*. [Online]. Available: <http://rOk.us/graphics/kodak/>
- [12] P. Hao, Y. Li, Z. Lin, and E. Dubois, "A geometric method for optimal design of color filter arrays," *IEEE Trans. Image Process.*, vol. 20, no. 3, pp. 709–722, Mar. 2011.
- [13] C. Bai, J. Li, Z. Lin, and J. Yu, "Automatic design of color filter arrays in the frequency domain," *IEEE Trans. Image Process.*, vol. 25, no. 4, pp. 1793–1807, Apr. 2016.
- [14] D. Alleysson, S. Stüssstrunk, and J. Héault, "Linear demosaicing inspired by the human visual system," *IEEE Trans. Image Process.*, vol. 14, no. 4, pp. 439–449, Apr. 2005.
- [15] K. Hirakawa and P. J. Wolfe, "Spatio-spectral color filter array design for optimal image recovery," *IEEE Trans. Image Process.*, vol. 17, no. 10, pp. 1876–1890, Oct. 2008.
- [16] L. Condat, "A new color filter array with optimal properties for noiseless and noisy color image acquisition," *IEEE Trans. Image Process.*, vol. 20, no. 8, pp. 2200–2210, Aug. 2011.
- [17] L. Zhong, S. Cho, D. Metaxas, S. Paris, and J. Wang, "Handling noise in single image deblurring using directional filters," in *Proc. IEEE Conf. Comput. Vis. Pattern Recognit.*, Jun. 2013, pp. 612–619.
- [18] Z. Hu, S. Cho, J. Wang, and M.-H. Yang, "Deblurring low-light images with light streaks," in *Proc. IEEE Conf. Comput. Vis. Pattern Recognit.*, Jun. 2014, pp. 3382–3389.
- [19] O. Whyte, J. Sivic, and A. Zisserman, "Deblurring shaken and partially saturated images," *Int. J. Comput. Vis.*, vol. 110, no. 2, pp. 185–201, Nov. 2014.
- [20] H. Liu, X. Sun, L. Fang, and F. Wu, "Deblurring saturated night image with function-form kernel," *IEEE Trans. Image Process.*, vol. 24, no. 11, pp. 4637–4650, Nov. 2015.
- [21] P. Chatterjee, N. Joshi, S. B. Kang, and Y. Matsushita, "Noise suppression in low-light images through joint denoising and demosaicing," in *Proc. IEEE Conf. Comput. Vis. Pattern Recognit.*, Jun. 2011, pp. 321–328.
- [22] D. Khashabi, S. Nowozin, J. Jancsary, and A. W. Fitzgibbon, "Joint demosaicing and denoising via learned nonparametric random fields," *IEEE Trans. Image Process.*, vol. 23, no. 12, pp. 4968–4981, Dec. 2014.
- [23] J. Han, J. Yue, Y. Zhang, and L. Bai, "Local sparse structure denoising for low-light-level image," *IEEE Trans. Image Process.*, vol. 24, no. 12, pp. 5177–5192, Dec. 2015.
- [24] T. Klatzer, K. Hammernik, P. Knöbelreiter, and T. Pock, "Learning joint demosaicing and denoising based on sequential energy minimization," in *Proc. IEEE Int. Conf. Comput. Photogr.*, May 2016, pp. 1–11.
- [25] G. B. Heim, J. Burkepile, and W. W. Frame, "Low-light-level EMCCD color camera," *Proc. SPIE*, vol. 6209, p. 62090F, May 2006.
- [26] S. Ugawa, T. Azuma, T. Imagawa, and Y. Okada, "Image reconstruction for high-sensitivity imaging by using combined long/short exposure type single-chip image sensor," in *Proc. Asian Conf. Comput. Vis.*, Nov. 2010, pp. 641–652.
- [27] S. Wang, T. Hou, J. Border, H. Qin, and R. L. Miller, "High-quality image deblurring with panchromatic pixels," *ACM Trans. Graph.*, vol. 31, no. 5, pp. 120:1–120:11, 2012.
- [28] D. Sugimura, T. Mikami, H. Yamashita, and T. Hamamoto, "Enhancing color images of extremely low light scenes based on RGB/NIR images acquisition with different exposure times," *IEEE Trans. Image Process.*, vol. 24, no. 11, pp. 3586–3597, Nov. 2015.
- [29] D. Zhang and X. Wu, "Color demosaicing via directional linear minimum mean square-error estimation," *IEEE Trans. Image Process.*, vol. 14, no. 12, pp. 2167–2178, Dec. 2005.
- [30] K. Miettinen, *Nonlinear Multiobjective Optimization*, vol. 12. New York, NY, USA: Springer, 1998.
- [31] Y. Li, P. Hao, and Z. Lin, "Color filter arrays: Representation and analysis," Dept. Comput. Sci., Queen Mary Univ. London, London, U.K., Tech. Rep. no. RR-08-04, 2008.
- [32] (Jan. 29, 2015). *Rethinking Color Cameras*. [Online]. Available: <http://vision.seas.harvard.edu/colorsensor/>
- [33] P. V. Gehler, C. Rother, A. Blake, T. Minka, and T. Sharp, "Bayesian color constancy revisited," in *Proc. IEEE Conf. Comput. Vis. Pattern Recognit.*, Jun. 2008, pp. 1–8.
- [34] L. Shi and B. Funt, *Re-Processed Version of the Gehler Color Constancy Dataset of 568 Images*, accessed on Oct. 12, 2013. [Online]. Available: <http://www.cs.sfu.ca/~colour/data/>
- [35] D. Menon and G. Calvagno, "Regularization approaches to demosaicing," *IEEE Trans. Image Process.*, vol. 18, no. 10, pp. 2209–2220, Oct. 2009.
- [36] L. Condat, "A generic variational approach for demosaicing from an arbitrary color filter array," in *Proc. IEEE Int. Conf. Image Process.*, Nov. 2009, pp. 1625–1628.
- [37] J. Gu, P. J. Wolfe, and K. Hirakawa, "Filterbank-based universal demosaicing," in *Proc. IEEE Int. Conf. Image Process.*, Sep. 2010, pp. 1981–1984.
- [38] M. Singh and T. Singh, "Linear universal demosaicing of regular pattern color filter arrays," in *Proc. IEEE Int. Conf. Acoust., Speech Signal Process.*, Mar. 2012, pp. 1277–1280.
- [39] E. Dubois, "Frequency-domain methods for demosaicing of Bayer-sampled color images," *IEEE Signal Process. Lett.*, vol. 12, no. 12, pp. 847–850, Dec. 2005.
- [40] B. Leung, G. Jeon, and E. Dubois, "Least-squares luma-chroma demultiplexing algorithm for Bayer demosaicing," *IEEE Trans. Image Process.*, vol. 20, no. 7, pp. 1885–1894, Jul. 2011.
- [41] Z. Lin, R. Liu, and Z. Su, "Linearized alternating direction method with adaptive penalty for low-rank representation," in *Proc. Adv. Neural Inf. Process. Syst.*, vol. 2. 2011, pp. 612–620.



Jia Li received the B.S. degree in mathematics and the M.S. degree in computer science from Zhengzhou University, Zhengzhou, China, in 2007 and 2012, respectively. He is currently pursuing the Ph.D. degree with the Beijing Key Laboratory of Traffic Data Analysis and Mining, School of Computer and Information Technology, Beijing Jiaotong University. His research interest is image processing.



Chenyan Bai received the B.E. and M.S. degrees from Hebei University, Baoding, China, in 2008 and 2011, respectively, and the Ph.D. degree from Beijing Jiaotong University, Beijing, China, in 2016, all in computer science. She is currently an Assistant Professor with the Beijing Advanced Innovation Center for Imaging Technology, College of Information Engineering, Capital Normal University, Beijing. Her research interests include image processing and machine learning.



Jian Yu received the B.S. and M.S. degrees in mathematics and the Ph.D. degree in applied mathematics from Peking University, Beijing, China, in 1991, 1994, and 2000, respectively. He is currently a Professor with the School of Computer and Information Technology and the Director of the Beijing Key Laboratory of Traffic Data Analysis and Mining, Beijing Jiaotong University. His research interests include machine learning, image processing, and pattern recognition.



Zhouchen Lin (M'00–SM'08) received the Ph.D. degree in applied mathematics from Peking University in 2000. He was a Chair Professor with Northeast Normal University. He is currently a Professor with the Key Laboratory of Machine Perception (Ministry of Education), School of Electronics Engineering and Computer Science, Peking University. His research interests include computer vision, image processing, machine learning, pattern recognition, and numerical optimization. He is an IAPR Fellow. He is an Associate Editor of the IEEE TRANSACTIONS ON PATTERN ANALYSIS AND MACHINE INTELLIGENCE and the *International Journal of Computer Vision*.